Effects of High-Dose Microbeam Irradiation on Tumor Microvascular Function and Angiogenesis

Andrew N. Fontanella,[a,1,2] Mary-Keara Boss,[b,2] Michael Hadsell,[c,3] Jian Zhang,[c,d,4] Thies Schroeder,[e] Katherine G. Berman,[f] Mark W. Dewhirst,[a,e,5,6] Sha Chang[c,d,5] and Gregory M. Palmer[e,5]

[a] Department of Biomedical Engineering, Duke University, Durham, North Carolina; [b] Department of Molecular Biomedical Sciences, North Carolina State University, Raleigh, North Carolina; [c] Departments of Physics and Astronomy, and [d] Radiation Oncology, University of North Carolina-Chapel Hill; [e] Department of Radiation Oncology, Duke University Medical Center, Durham, North Carolina; and [f] Veterinary Biosciences, School of Veterinary Medicine, University of Glasgow, Glasgow, Scotland

Fontanella, A. F., Boss, M-K., Hadsell, M., Zhang, J., Schroeder, T., Berman, K. G., Dewhirst, M. W., Chang, S. and Palmer, G. M. Effects of High-Dose Microbeam Irradiation on Tumor Microvascular Function and Angiogenesis. *Radiat. Res.* 183, 147–158 (2015).

Microbeam radiation therapy (MRT) is a form of cancer treatment in which a single large dose of radiation is spatially fractionated in-line or grid-like patterns. Preclinical studies have demonstrated that MRT is capable of eliciting high levels of tumor response while sparing normal tissue that is exposed to the same radiation field. Since a large fraction of the MRT-treated tumor is in the dose valley region that is not directly irradiated, tumor response may be driven by radiation bystander effects, which in turn elicit a microvascular response. Differential alterations in hemodynamics between the tumor and normal tissue may explain the therapeutic advantages of MRT. Direct observation of these dynamic responses presents a challenge for conventional *ex vivo* analysis. Furthermore, knowledge gleaned from *in vitro* studies of radiation bystander response has not been widely incorporated into *in vivo* models of tumor radiotherapy, and the biological contribution of the bystander effect within the tumor microenvironment is unknown. In this study, we employed noninvasive, serial observations of the tumor microenvironment to address the question of how tumor vasculature and HIF-1 expression are affected by microbeam radiotherapy. Tumors (approximately 4 mm in diameter) grown in a dorsal window chamber were irradiated in a single fraction using either a single, microplanar beam (300 micron wide swath) or a wide-field setup (whole-window chamber) to a total dose of 50 Gy. The tumors were optically observed daily for seven days postirradiation. Microvascular changes in the tumor and surrounding normal tissue differed greatly between the wide-field and microbeam treatments. We present evidence that these changes may be due to dissimilar spatial and temporal patterns of HIF-1 expression induced through radiation bystander effects. © 2015 by Radiation Research Society

INTRODUCTION

Recent advances in radiation physics have brought the field of microbeam radiotherapy (MRT) closer to clinical application. This technology typically delivers spatially fractionated doses of hundreds of gray (Gy) in repeated, submillimeter microplanar patterns separated by wider regions that receive very little (1–10%) dose. Because this technique is in preclinical development, these doses and geometries vary greatly between studies, and ideal treatment schemes are currently being investigated (*1–3*).

MRT studies have reported specific tumor cell kill with relatively minimal normal tissue effects. One hypothesis that explains this normal tissue resistance involves a greater capacity for morphologically and functionally normal vasculature to recover from spatially fractionated treatment, relative to the unregulated, immature vasculature associated with tumors (*4*). However, this proposal has yet to be validated. It is likely that the tissue response to microbeam treatment is temporally complex, making it difficult to discern the kinetics of the tissue response solely from *ex vivo* pathologic analysis.

Although abnormal in structure, tumor-associated vessels are the source of oxygen delivery, and it is well established that the aberrant vasculature characteristics contributes to tumor hypoxia (*5*). Structural and functional alterations due to radiation damage may further contribute to changes in tumor oxygenation (*6, 7*). Tumor hypoxia has been

associated with poor outcomes in a number of clinical studies (*8, 9*). Furthermore, improvements in oxygenation during fractionated radiotherapy are associated with differential outcomes when compared to tumors that do not reoxygenate (*10–12*). It is not known how hypoxia is altered after microbeam radiotherapy. This study establishes these effects for microbeam compared with whole-window radiotherapy when both modalities deliver the same dose.

We have previously shown that the vascular response to radiation exposure in tumors is mediated by upregulation of HIF-1, a transcription factor responsible for regulating hypoxia-related gene expression. HIF-1 regulates genes that drive angiogenesis, tumor cell invasiveness, metastasis and proliferation (*13*). HIF-1 is a heterodimer, consisting of constitutively produced HIF-1α and HIF-1β. HIF-1α is normally kept at low levels in the presence of oxygen via proteosomal degradation mediated by the VHL complex. However, exposure to radiation can cause stabilization of HIF-1α expression through a number of mechanisms (*6*), leading to upregulation of many downstream genes.

In this study we used the dorsal skinfold window chamber model to serially compare the vascular effects of whole-tumor versus microbeam radiotherapy. This animal model is uniquely capable of offering high-resolution images of the tumor and associated vasculature at optical wavelengths. Furthermore, it facilitates serial noninvasive measurements of the tumor microenvironment, allowing for the observation of temporally evolving aspects of tumor growth and treatment response, including vascular disruption, perfusion, angiogenesis and the regulation of HIF-1 expression (via fluorescent protein reporters) (*14*). These advantages are particularly important for a thorough understanding of microphysiological radiation effects, since no other *in vivo* model effectively facilitates the tracking of temporal changes at the level of single microvessels.

Investigation of tumor vascular parameters through image analysis is technically challenging. Manual methods of extracting quantitative image data are generally inefficient and are prone to introducing user bias. Therefore, we have developed automated methods for quantifying vascular functional and structural changes after irradiation (*15*). Tumor response is tracked through serial measurements over a week-long time course, and derived microenvironmental parameters are statistically evaluated. Here we show that spatial application of dose by a single microbeam elicits differing effects on the tumor microvasculature through unique patterns of disruption. Furthermore, we demonstrate that HIF-1 signaling in adjacent nonirradiated tumor regions is associated with this response.

MATERIALS AND METHODS

4T1-RFP-GFP Cell Line

A genetically engineered 4T1 murine mammary carcinoma cell line was used for this study (*16*). This line was stably transfected with a plasmid vector encoding a green fluorescent protein (GFP) reporter

(*17*). Expression of GFP in the cell is driven by a HIF-1-modulated hypoxia responsive element (HRE). An HRE is a DNA sequence in the promoter region of a gene that HIF-1 binds with to induce enhanced gene transcription. Thus HIF-1 expression within a tumor grown from this line can be directly visualized and quantified through the intensity of the GFP signal. This line was also stably transfected with a red fluorescent protein (RFP) gene under control of the cytomegalovirus (CMV) promoter. Expression of RFP is constitutive (always active) and is used to visualize the spatial location and extent of the tumor.

Dorsal Window Chamber Preparation

A thorough explanation of the dorsal window chamber surgical procedure is provided in previously published articles (*14, 18*). Briefly, nude mice were anesthetized using a ketamine/xylazine preparation and the surgical area was disinfected using Exidine® and ethanol. In each mouse, a circular incision, 12 mm in diameter, was made in the loose skin of the dorsal surface. The skin and underlying connective tissue were removed completely. The dorsal skin was pinched up to form a skin fold, which exposed the dermal tissue on the opposite side of the area of excised skin. The incision was aligned with a hole cut into a specially constructed titanium frame, which was then sutured onto the animal to form a stable window into the underlying tissue. Approximately 2×10^4 4T1-GFP-RFP cells suspended in serum-free media were injected beneath the exposed fascial plane. A sterile glass coverslip was then inserted into the titanium frame to form an airtight, optically-accessible window into the inoculated tumor and surrounding tissue. Irradiation was carried out one week after tumor cell transplant, when solid, vascularized tumors 3–5 mm in diameter had been formed. We have shown previously that these tumors are hypoxic and express HIF-1 at this size range (*19–21*).

Optical Data Acquisition and Image Processing

A detailed description of the data acquisition methods and image processing algorithms are provided in the supplemental methods. Briefly, hyperspectral image series were used to spectrally separate oxy/deoxy hemoglobin components for analysis of hemoglobin O_2 saturation (*22*). Total hemoglobin data (oxy + deoxy hemoglobin) were used to measure vascular hemoglobin concentrations. We also used the hyperspectral system to separate fluorescent reporters of interest (RFP and GFP) from tissue autofluorescence to more accurately quantify levels of expression.

Total hemoglobin images were used to quantify vascular structural features (i.e., vessel centerlines, diameters, branch points) using the described vessel segmentation/skeletonization algorithm. Video images of blood flow within the tumor were used to map and quantify flow speed and direction. The algorithm used for this procedure is briefly described in the supplemental methods, and more thoroughly presented in a previously published article (*23*).

Window Chamber Tumor Irradiation

A nanotechnology-based X-ray experimental irradiator specifically designed to produce microbeam radiation was used for this study (*24–26*). More detailed information about the dosimetry and geometry of this microbeam radiation technique can be found in refs. (*24–26*). This novel irradiation system utilizes a line source design (instead of the conventional point source) that is optimized to produce the highest beam intensity for the microbeam. Anesthetized mice were placed in the system with their titanium frames immobilized on a heated stage. Animals treated in the microbeam tumor irradiation group were exposed to 50 Gy at a dose rate of 1 Gy/min as 160 kVp photons passed through a collimator to produce a single full-width half-max (FWHM) 300 μm wide microbeam through the middle of the tumor (Fig. 1A). Radiation intensity fell off sharply, with areas greater than 200 μm from the beam centerline receiving less than 10% of the
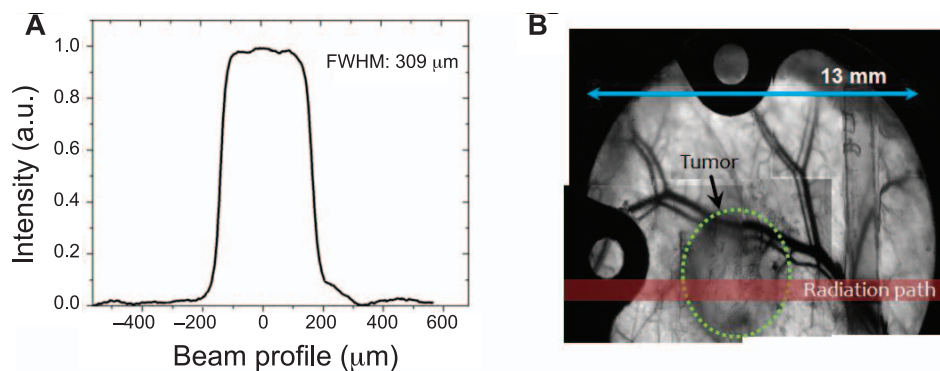
FIG. 1. Microbeam irradiation. Panel A: The radiation intensity profile had a full-width half-max of approximately 300 μm. Panel B: Window chamber-grown tumors were irradiated with the source situated above the window. The radiation penetrated the tumor orthogonally to the tissue plane. The length of the beam spanned the 13 mm diameter window.

maximum dose. This beam spanned the width of the window along its centerline, and its track was visualized using a radiation-sensitive film glued to the front of the glass coverslip (Fig. 1B). For the whole tumor irradiation group, the microbeam collimator was removed, and the entire window was irradiated while sparing the rest of the animal's body. In both irradiation procedures, the delivered dose was 50 Gy (25, 27). The dose of 50 Gy was selected based on preliminary experiments whereby a single microbeam of radiation induced a tumor vascular response and the corresponding wide-field exposure allowed sufficient tissue viability for biologic comparisons. A mock-irradiated group was also used as a control.

Window Chamber Imaging Schedules

The methods outlined above were used to optically observe and quantify changes in HIF-1 and vascular response after irradiation. Animals were imaged approximately 2 h prior to irradiation, 2 h postirradiation and each day following through seven days postirradiation. For each time point, the windows were imaged using the hyperspectral system described above, with illumination, filtering and exposure parameters adjusted to capture total hemoglobin/saturation, GFP fluorescence emission and RFP fluorescence emission. The tumor and surrounding area were imaged at 2.5× magnification for these optical components, and it was from these images that the regions of tumor core, rim and tumor-associated normal tissue were identified (Supplementary Fig. S1; http://dx.doi.org/10.1667/RR13712.1.S1). Video images were also collected in a 24 Hz, 128 frame series at 5× magnification to capture the movement of discrete red blood cells as they moved through the vasculature.

Statistical Analysis

After processing the acquired data for the extraction of microenvironmental parameters, median values were calculated within each spatial region at each time point, for each animal. We then calculated the linear fit of the change in median values for each region within each animal. The slope of this line represented the rate of change of any particular parameter over the treatment time course. Within each region, slopes were grouped according to treatment type (i.e., microbeam, whole or mock irradiation, with N = 6, 6 and 5, respectively), and statistical analysis using one-way ANOVA was used to detect significant treatment effects. The Tukey-Kramer method was then applied to these results to detect pair-wise statistical significance between treatment groups. We also calculated the time-averaged GFP expression in the tumor rim as a percentage of overall expression, and applied the same statistical tests for significant differences between treatment groups. In all figures, error bars represent the standard error of the mean.

Histological Analysis

After the completion of imaging on day 7, animals were euthanized and their window chamber tumors were immediately extracted and snap frozen. The frozen tumors were then processed by routine methods and multiple (at least four) successive 4 μm sections were hematoxylin and eosin (H&E) stained. After histological preparation, cellular features were evaluated by a pathologist who was blinded to the treatment groups at the time of assessment.

Animal Welfare Statement

All procedures described in this study were performed in accordance with animal welfare protocols approved by Duke University's Institutional Animal Care and Use Committee.

RESULTS

Vascular Structure

Qualitative observation of tumors irradiated with the single microbeam showed a consistent pattern of vascular expansion after radiation. Angiogenic vessels were preferentially directed into the postirradiation beam path (Fig. 2). In comparison, neither the wide-field nor the mock-treated tumors showed a similar effect; in these cases, angiogenesis did occur, but it was generally less profound and showed no particular directional preference.

Using one-way ANOVA/Tukey-Kramer analysis as described above, we observed no significant differences in the rate of change of intratumoral vascular length density or percentage vascular area over time among any of the treatment groups (Fig. 3A and C). However, within the tumor-associated normal tissue, the wide-field group displayed a significantly decreased vascular length density by the end of the time course relative to the mock group ($P = 0.0147$) and a near significant decrease relative to the microbeam group ($P = 0.054$) (Fig. 3B). By day 7, the wide-field group also showed a significantly greater decrease in vascular area within the tumor-associated normal tissue, compared to either the mock or microbeam groups ($P = 0.0124$ and $P = 0.0222$) (Fig. 3D). These data indicate a radiation-induced vascular regression within the tumor-
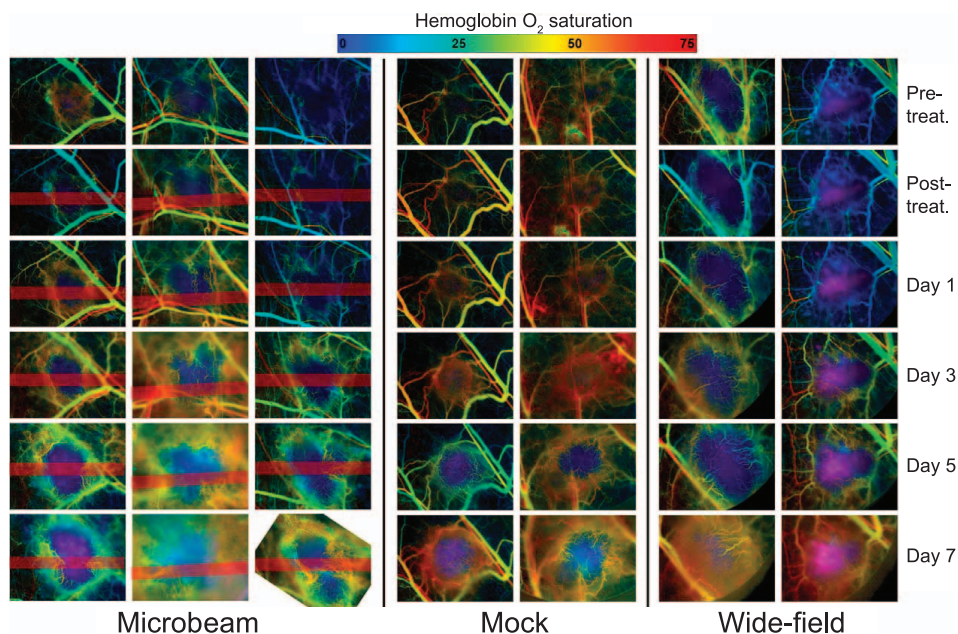
FIG. 2. Patterns of angiogenesis after irradiation: Representative images of tumor-associated vasculature overlaid with hemoglobin oxygen saturation values. Three different microbeam, two different mock, and two different wide-field windows are shown. Longitudinal imaging at time points prior to irradiation through day 7 allowed visualization of the changes in tumor vascularization patterns. Over time, the patterns of vascular expansion in the microbeam group indicated a preferential infiltration of the irradiated portion of the tumor (arrows, with irradiated portion highlighted in red). Compared to the microbeam group, the angiogenic response within the mock and wide-field groups showed no apparent localized patterns of expansion or changes in vessel orientation. Vessels in these groups generally radiate inward from the tumor edge without notable variations in vessel density.
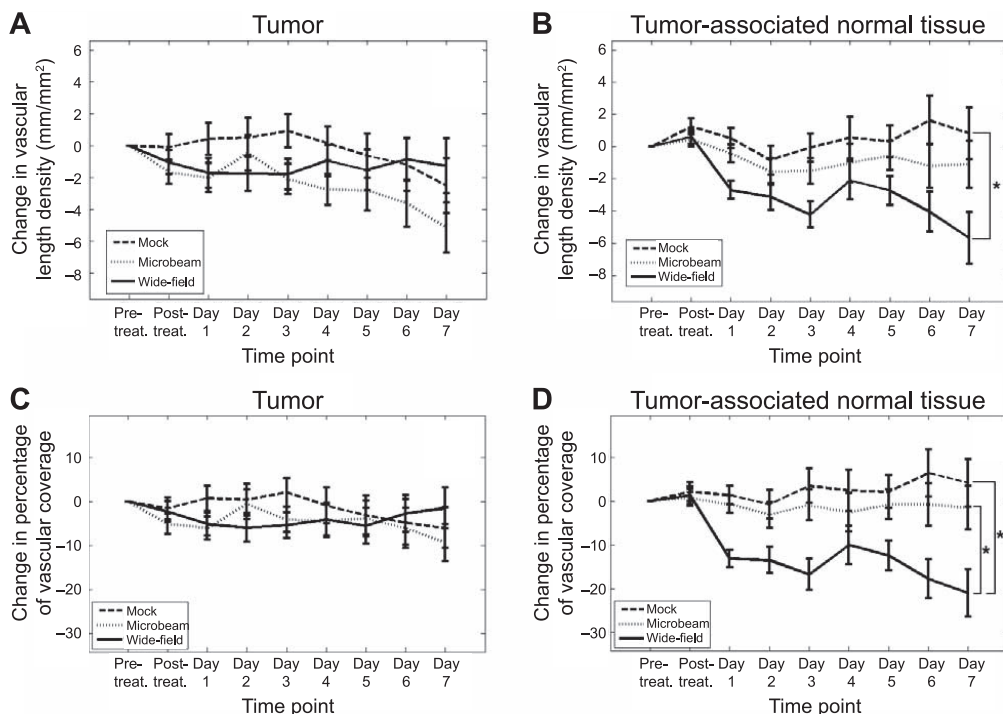

FIG. 3. Changes in vascular length density and percentage vascular coverage over time. No significant differences in the rate of change in either parameter were observed among the treatment groups within the tumor itself (panels A and C). Within the tumor-associated normal tissue, however, the wide-field group showed a significant drop in vascular length density relative to the mock group (panel B) ($P = 0.0147$). A significant drop in the wide-field group's percentage vascular coverage was observed on the final day relative to both mock and microbeam groups (panel D) ($P = 0.0124$ and $P = 0.0222$, respectively)
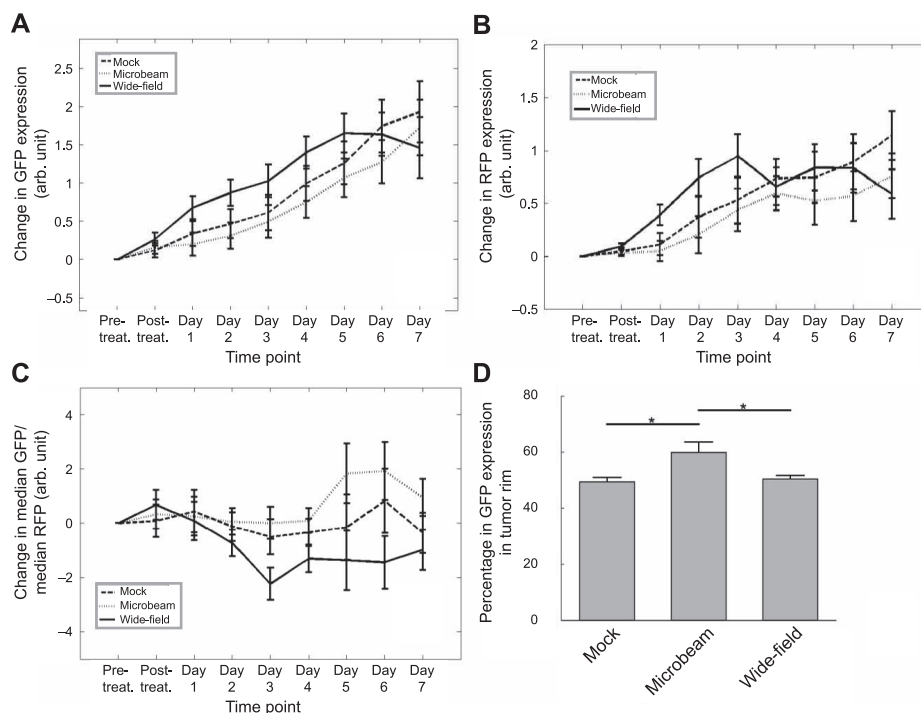
FIG. 4. Changes in fluorescent reporter expression over time. Both the microbeam and mock group showed a consistent increase in GFP (indicating HIF-1) over time, whereas the wide-field group saw a decay in expression around day 5 (panel A). A similar decay was observed in the expression of RFP (constitutively expressed) (panel B). When RFP was used to control for total protein expression, the ratio of median GFP to median RFP showed that the microbeam group is the only one to show a notable increase in relative expression of GFP (panel C). Within the tumor rim, GFP expression was proportionally higher in the microbeam group than in the mock or wide-field groups (panel D). ($P = 0.0323$ and $P = 0.0425$, respectively)

associated normal tissue region of the wide-field group. The lack of effect within this region in the mock and microbeam groups may be due to the fact that most of the tissue in these regions received virtually no radiation dose (microbeam), or no radiation at all in the mock controls.

Microvessel Perfusion and Flow Direction

We next analyzed hemodynamics from videos to determine microvessel blood flow patterns using our previously described mapping algorithm (*15*). Blood flow was maintained within the vascular network after treatment. We did observe patterns of vascular reorganization within the microbeam group, however. Consistent with structural data presented above, vessels tended to branch out into the region of radiation exposure in the microbeam group. This was particularly notable in one tumor, where vessels initially running largely parallel to the beam path on the day of irradiation changed their orientation to a more perpendicular orientation in just a few days (Supplementary Fig. S2; http://dx.doi.org/10.1667/RR13712.1.S1).

Spatial and Temporal Patterns of HIF-1 Expression

Median HIF-1-GFP signal consistently increased at each successive time point in the mock and single-microbeam groups (Fig. 4A). This constant increase was also observed in the wide-field group through day 5, however at day 6 and

7 the signal decreased from the preceding day. To determine whether this effect was due to cell death we also measured changes in RFP expression (Fig. 4B). Since RFP serves as a constitutive reporter, the expression of this protein should serve as a concurrent indicator of the number of viable cells in the tumor. We therefore defined the ratio of GFP:RFP expression, as GFP expression *per viable tumor cell*. Tumor-wide GFP:RFP expression showed no statistically significant trends (Fig. 4C). However, the GFP:RFP expression in the tumor rim (integrated over all time points) was significantly higher in the microbeam group than in either the mock or wide-field groups ($P = 0.0323$ and $P = 0.0425$, respectively) (Fig. 4D).

Alterations in Vascular Hemoglobin Concentration

The overall change in vascular hemoglobin concentration within the tumor was highest in the microbeam group (Fig. 5A). The most notable rate of change began on the third day postirradiation. The effect was not noted in the tumor-associated normal tissue (Fig. 5B), but was prominent in the tumor itself, both within the rim (Fig. 5C) and core (Fig. 5D).

The rate of change in hemoglobin concentration within the tumor was significantly different for the wide-field group compared to the microbeam group ($P = 0.0243$) (Fig. 6A). When the time course was split into two segments
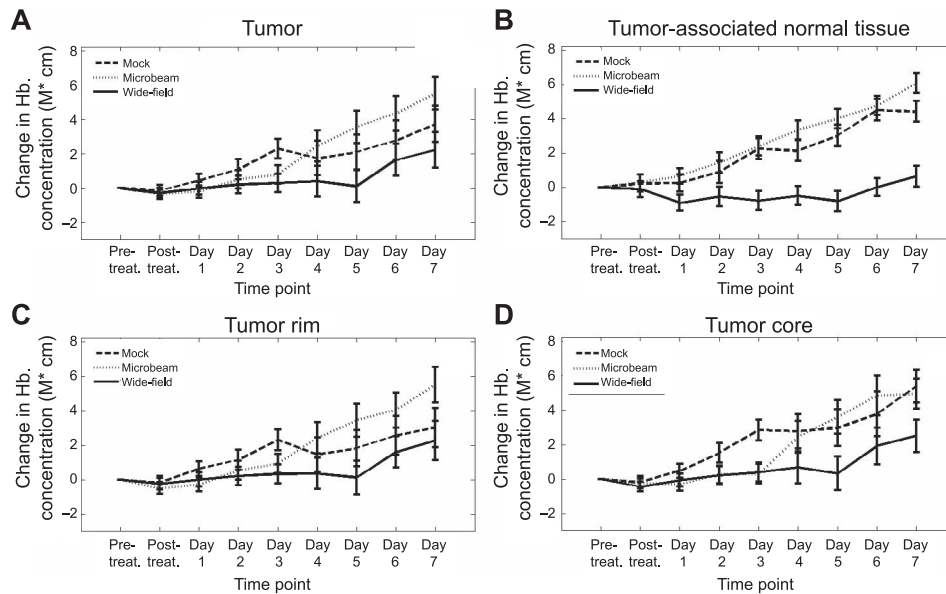
FIG. 5. Changes in vascular hemoglobin concentration over time. Microbeam irradiation elicited a biphasic effect on vascular hemoglobin concentration within the tumor (panel A). Over the first four days of the time course, hemoglobin concentration remained relatively constant, compared to the marked increase later seen over the last four days. In comparison, the feeding vessels of the tumor-associated normal tissue maintained a more constant rate of change that did not seem to be affected by microbeam treatment (panel B). These vessels may have helped initiate the vascular response seen the tumor rim, and to a larger extent, the tumor core (panels C and D).

(pretreatment – day 3 and day 3–7), the rate of change in hemoglobin concentration was not significantly different among any groups within the first timeframe (Fig. 6B). Within the second timeframe, however, the rate of change within the microbeam group was significantly higher than either the mock or wide-field groups ($P = 0.0285$ and $P = 0.0270$, respectively) (Fig. 6C). Only the microbeam group showed a significant difference in rates between the two timeframes ($P = 0.0215$) (Fig. 6D).

Alterations in Hemoglobin Oxygen Saturation (Wide-Field Group)

Hemoglobin saturation was tracked in the three different treatment groups (Fig. 7A). Concurrent with the drop in HIF-1 reporter expression after wide-field irradiation, we observed an increase in hemoglobin oxygen saturation relative to the mock and microbeam groups persisting through day 6 and 7 ($P = 0.0039$ and $P = 0.0035$, respectively) (Fig. 7B).

Histological Analysis of Tumors

Representative images of the tumors are shown in Supplementary Fig. S3 (http://dx.doi.org/10.1667/ RR13712.1.S1). Histologic findings varied between the three treatment groups. In the mock group, the neoplastic nodules were composed of haphazardly arranged pleomorphic polygonal to spindle-shaped cells with moderate anisocytosis and anisokaryosis. The number of mitotic figures in the mock group ranged from 30 to 55 per 10 high

power fields (40×). Also observed were randomly scattered, patchy areas of lytic necrosis (affecting anywhere from less than 5% of the mass to up to 20% of the mass in different animals and in different planes of section).

Relative to the mock group, the neoplastic cells of the wide-field group were extremely pleomorphic and very large. Individual cells were up to 50 μm in diameter. There were frequent multinucleated cells with up to 8 nuclei in a single cell. Severe anisocytosis and anisokaryosis were noted, with some nuclei up to 8 times larger than others. The mitotic index ranged from 12–25 mitotic figures per 10 high-power fields (40×), and over half of the mitotic figures were bizarre. Patchy foci of lytic necrosis ranged from less than 5% up to 25% of the mass.

Within the microbeam-irradiated tumors, two distinct phenotypes were observed. In most of the tissue sections approximately 80% of the neoplastic mass resembled the mock group of tumors. However, the remaining 20% of the tissue was composed of a central or slightly off-center, roughly linear band of neoplastic tissue that resembled the wide-field group of irradiated masses with larger, more pleomorphic cells. This band of tissue ranged from about 0.2–0.5 mm in diameter. Foci of lytic necrosis in both of the neoplastic populations ranged from less than 5% up to 20% of the mass.

In summary, mock-treated tumors showed a cellular phenotype typical for this particular cell line. Patchy areas of necrosis were observed, presumably in the areas of severe hypoxia. The number of mitotic cells present in the tumor indicated viability and continued patterns of growth. In
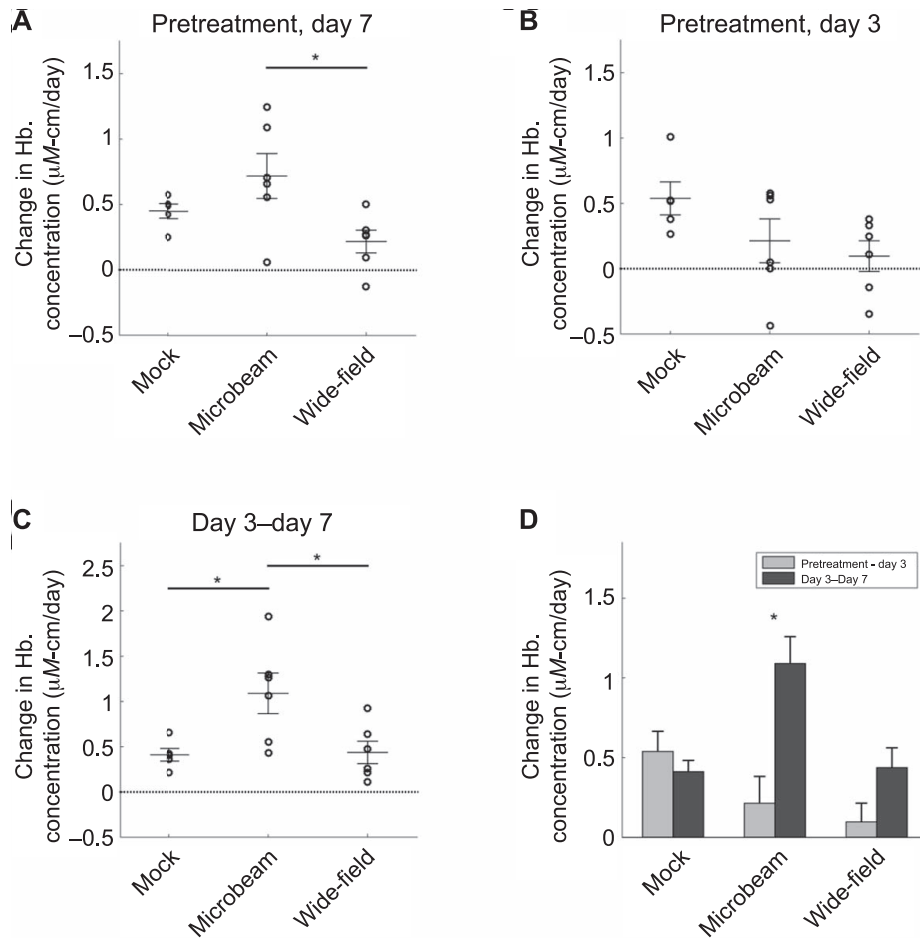
FIG. 6. Rates of change in vascular hemoglobin concentration within tumors. Both mock- and microbeam-treated tumors showed a consistent increase in vascular hemoglobin concentration over the entire time course. In contrast, concentrations within wide-field-treated tumors tended to remain static (panel A). Between the day of treatment and the third day post, no significant differences in the rate of change were observed among the treatment groups (panel B). From day 3–7, however, the microbeam group had a rate of change significantly greater than either the mock or wide-field groups (panel C) ($P = 0.0285$ and $P = 0.0270$, respectively). When the rates of change were compared over the two timeframes, only the microbeam-treated tumors showed a significant change (panel D) ($P = 0.0215$).
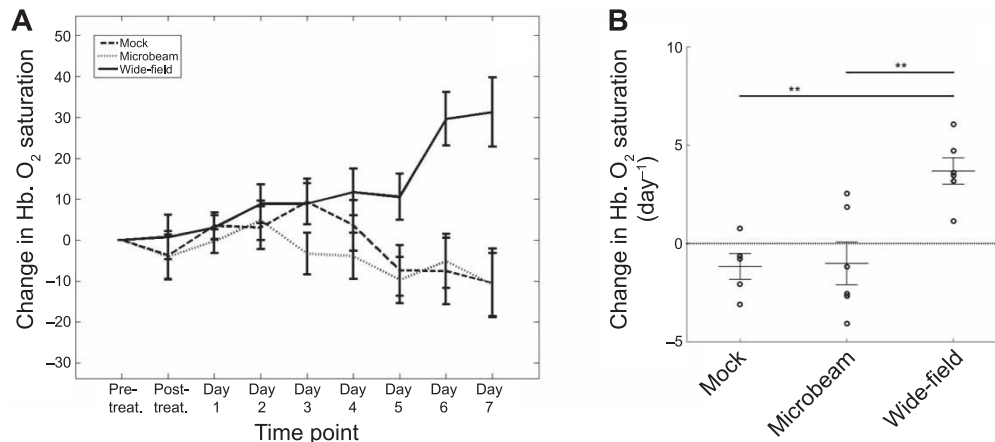

FIG. 7. Changes in hemoglobin O_2 saturation within the tumor-associated vasculature. Within the wide-field group, hemoglobin oxygen saturation increased abruptly over the last few days of the time course (panel A). The average rate of change was significant within the wide-field group when compared to either mock or microbeam treatments (panel B) ($P = 0.0039$ and $P = 0.0035$, respectively).

contrast, tumor cells in the whole-field group showed indications of radiation-induced damage; giant multinucleated cells and aberrant mitosis were commonly observed. The microbeam-treated tumors showed a linear band through the tumor with the same phenotype as the wide-field group. The width of this zone was consistent with the width and orientation of the microbeam. Cells outside of the irradiated region were identical to the mock-treated tumors.

DISCUSSION

The data presented here compare the effects of 50 Gy irradiation, using either wide-field or microbeam techniques (with mock-treated controls), on tumors grown in the skin-fold window chamber. To evaluate the effects of the various treatments on the tumor microenvironment, we employed the methods described above on images collected daily over the pre- and post-treatment time course. Data on vessel structure and function indicated the extent that radiation exposure caused vascular disruption within the tumor, as well as determine its capacity for recovery in the days afterwards. Measurements of hemoglobin concentration and hemoglobin saturation provided complementary information on the perfusion and oxygen transport capabilities of the affected vasculature. Furthermore, regulation of HIF-1 expression was tracked and quantified through the observation of GFP expression. H&E histology was performed after tumors were extracted on the final day of imaging, and these results confirmed that the differing irradiation techniques produced distinctive patterns of cell death within the tumor: diffuse cellular damage and death in the wide-field-irradiated tumors, and linearized, focal cell damage and death in the microbeam-irradiated tumors. These comprehensive data provide multi-parametric assessment of physiologic perturbation and recovery in the tumors that were mock treated, microbeam and wide-field irradiated. Through automated demarcation of the predefined tumor regions, the spatial dynamics of these effects were also elucidated.

Over the eight day time course, we found that exposure to 50 Gy causes: 1. unique physiologic changes in different tumor/normal tissue regions and 2. differential effects between wide-field and microbeam irradiations. We propose that microbeam irradiation causes an upregulation in HIF-1 in the nonirradiated portions of the tumor through bystander mechanisms. HIF-1, in turn, potentiates vascular recovery. In contrast, wide-field-treated tumor irradiation results in widespread cell death. Cell death contributes to reoxygenation because a lowered cell density will reduce oxygen consumption. A visual representation of this proposed model is featured in Supplementary Fig. S4 (http://dx.doi.org/10.1667/RR13712.1.S1).

Wide-Field Irradiation

A decrease in vascular length density and percentage vascular coverage was observed after treatment in the tumor-associated normal tissue. In contrast, vascular density and percentage vascular coverage were unchanged in the tumor. The lack of change in hemoglobin concentration was in contrast with the other treatment groups, where concentrations increased over time. These results were interpreted as an inhibition of vascular growth due to the radiation treatment. The vessels that remained after treatment showed no apparent lack of functionality, however, as perfusion persisted there was no visible vascular stasis.

Hemoglobin oxygen saturation increased dramatically in the last days of the study. This effect suggested oxygen consumption had decreased. The pathologic data showed that there was widespread cell death, which would reduce oxygen consumption rate. These results are consistent with the prevailing theory that oxygenated cells are preferentially killed by radiation, freeing up oxygen for diffusion into formerly hypoxic tumor regions (6). Previously, we had shown that HIF-1 induction occurs coincidentally with reoxygenation after three daily fractions of 5 Gy in this tumor model (16). We observed a dissimilar trend here, however. As tumor oxygenation increased, HIF-1 decreased. The lack of HIF-1 induction was likely due to the very high radiation dose the tumor received. A substantially reduced number of viable cells would reduce HIF-1-driven GFP production. The concurrent drop in RFP expression supports this explanation, as well as the observation of widespread tumor cell death in histological samples.

Single-Microbeam Irradiation

Radiation was delivered by a 300 μm wide beam that cut through the tumor, leaving nonirradiated tumor volumes on either side. The geometry of this scheme resulted in relatively smaller fractions of the tumor rim and tumor-associated normal tissue receiving radiation. Histological analysis of the microbeam-treated tumors confirmed this pattern of radiation exposure, with a central linear region displaying radiation damage similar to the wide-field group, and an outer, nonirradiated mass with histological features similar to the mock-treated tumors.

No direct evidence of vessel depletion or loss of functionality was observed in the microbeam-irradiated group. In fact, changes in vascular length density and percentage vascular coverage after microbeam irradiation largely followed the same trend as mock-irradiated controls. A visual assessment of the pattern of vascular response reveals a pronounced angiogenic effect originating within the tumor-associated normal tissue along the radiation path.

Vascular function remained unaltered in the microbeam group, as assessed through maps of blood flow speed. Furthermore, we observed no significant alteration in hemoglobin oxygen saturation after treatment, suggesting that tumor oxygenation remained stable throughout the time course. Unique patterns of vascular remodeling were

highlighted in the flow direction maps, however. Here we observed that blood flow was redirected into the irradiated beam area. Thus, both functional and structural analyses of the vasculature indicate that microbeam irradiation leads to an increase in angiogenesis, enhancing the blood supply to irradiated tissue.

This vascular adaptation to localized radiation may be facilitated through HIF-1 expression, since it has been shown that HIF-1 expression is increased after radiation treatment (21). Spatial analysis showed that the primary area of HIF-1 expression was not within the irradiated tumor core. A relatively high amount of HIF-1 activity was found in the tumor rim and this increase was circumferential, rather than following the path of the microbeam treatment. These data provide indirect evidence that bystander signaling increases HIF-1 expression, which perhaps emanates from the irradiated area, into nonirradiated tumor tissues. The radiation bystander process is thought to be at least partially mediated through the radiation-induced production of free radicals (28, 29). Damage to mitochondria may further potentiate this oxidative stress (30). The production of the diffusible and long-lived reactive species, hydrogen peroxide and nitric oxide, have been prominently implicated in the bystander response (31). Bystander-affected cells have been shown to increase the production of both of these reactive species. Both hydrogen peroxide and nitric oxide, in turn, stabilize HIF-1 in the presence of oxygen (16, 32). Additionally, it has been shown that reactive oxygen species-mediated HIF-1 induction occurs on the transcriptional level and is dependent on NF-κB (33). Thus, the observation of increased HIF-1 expression in the rim, despite a lack of any direct damage from radiation, suggests that bystander signaling is active here. The increase in HIF-1 expression after microbeam treatment likely contributes to the angiogenic response because it upregulates expression of two proangiogenic cytokines, VEGF and angiopoeitin-2 (13).

The sharp increase in hemoglobin concentration beginning on the third day post treatment further implicates bystander-induced HIF-1 upregulation in the post-microbeam irradiation response. A primary effect of VEGF upregulation is an increase in vascular permeability. As a result of this change, plasma leakage into the interstitial space will cause microvascular hematocrit to rise. This is consistent with the postirradiation increase in hemoglobin concentration within the tumor.

Interpretation of Treatment Effects

The laboratories of Fuks and Kolesnick have theorized a model in which endothelial cell apoptosis serves as the primary mechanism dictating tumor radiation sensitivity after high doses per fraction (34). This alternative hypothesis challenges the classical model of tumor clonogenic cell death as the driving mechanism of radiation response (35). The relative role that vascular destruction plays in dictating tumor radiation response is controversial, however (34–39).

The data presented here do not support the hypothesis that vascular disruption occurs after high doses of radiation. Within the microbeam group the structural and functional characteristics of the vasculature as a whole did not change, relative to the pre-treatment data. Post-treatment initiation of a HIF-1 response in the tumor rim may have protected the tumor against vascular depletion through the angiogenic recruitment of blood vessels from the tumor-associated normal tissue. These results, however, compare the tumor microenvironmental effects of a single microbeam of radiation to nonirradiated (mock-treated) or wide-field irradiated tumors, which is not how this treatment will be deployed if given with therapeutic intent. The most common configuration used thus far has been multiple parallel microbeam paths that traverse tumor and normal tissue. In future studies, it will be important to examine how traditional parallel microbeam patterns used in MRT affect normal and tumor vascular function.

While angiogenesis is known to be a major factor in tumor-mediated vascular expansion, an alternative hypothesis presents vasculogenesis as the major factor after radiation therapy. In this model, high-dose irradiation of the tissue bed eradicates the vasculature within the treatment field. Vascular function is reestablished through the *de novo* (i.e., vasculogenic) formation of blood vessels. It has been shown that vasculogenesis is achieved through the infiltration of endothelial progenitor cells from the peripheral blood, assisted by bone marrow-derived myelomonocytes expressing MMP-9 (an extracellular matrix degrading enzyme) (40). This study was not designed to examine this mechanism, but the results do not preclude that both angiogenesis and vasculogenesis may play a combined role in vascular response after partial tumor irradiation.

The driving factor in microvessel survival and/or recovery after irradiation and the magnitude of this effect may be dependent upon the particular radiation-treatment scheme employed. Our results clearly indicate that vascular expansion is potentiated when the tumor is partially spared. We propose that this phenomenon is linked to both the vascular protective and angiogenic effect of HIF-1, and the unique pattern of expression observed in this scenario. HIF-1 was shown to be upregulated primarily in the tumor rim, which received relatively less radiation exposure than the tumor core. Thus, the data presented here provide evidence that tumor-mediated intercellular signals initiated in the lethally irradiated portion of the tumor core enable vascular recovery through the induced expression of HIF-1 in nonirradiated portions of the tumor. Following this indirect upregulation of HIF-1, a profound angiogenic and/or vasculogenic response is observed. To confirm this mechanistic link, quantification of native HIF-1 protein stabilization and induction of HIF-1 target proteins is warranted, as well as experimental elimination of reactive species and/or disruption of HIF-1 to demonstrate causality.

Owing to the known detrimental effects of HIF-1 with respect to tumor radioresistance (*13, 16, 32*), these observations provide evidence of possible detrimental effects after the inhomogeneous tumor irradiation inherent to spatially fractionated treatment, and thus strongly indicates the need for more research on the mechanisms behind the efficacy of MRT before moving forward to clinical trials. In addition, this vascular contribution to tumor radiation response may also play a major role in conventional therapies, such as IMRT, where a marginal miss (effectively a local spatially fractionated dose distribution) may produce similar effects. The importance of unintentional sparing of tumor margins is poorly understood, and may be largely determined by the vascular response, as seen here.

It is important to note, however, that the spatial modulation of dose in this study is simplistic compared to those typically employed in most spatial fractionation techniques, including MRT. Characteristically, MRT uses highly collimated, quasi-parallel arrays of X-ray microbeams of 50–600 keV in which a large array of thinner (25–75 microns wide), higher dose (in the order of 100 Gy) microbeams are employed and separated by wider (100–400 microns center to center) microplanar spaces (*41*) or larger scale minibeams (500–700 microns wide) (*42*); our study examines the tumor microenvironmental effects of a single microbeam of radiation. Specifically, we utilized a 300 μm wide microbeam through the tumor to administer 50 Gy with 160 kVp photons at a dose rate of 1 Gy/min. The ''valley dose'' in our arrangement with the single microbeam could be considered 300–400 μm from the beam centerline where the tissue would receive less than 1% of the maximum dose (Fig. 1A). Additionally, the radiation exposure for these experiments was administered at a lower dose rate (1 Gy/min) compared to synchrotron-based MRT systems (500–800 Gy/s) (*43*). Intercellular signaling factors in the more intricate geometries of spatial fractionation techniques may produce variable effects dependent upon geometry/dose-sensitive diffusion gradients (*43–46*). Notably, these preclinical MRT techniques have been associated with normal tissue sparing and tolerance, tumor targeting and maintenance of the normal microvasculature. Thus, evidence presented here may not necessarily be applicable to spatial fractionation techniques in general. However, these data are cause for concern regarding the long-term implications of unknown (as in the case of marginal misses) or poorly investigated spatial heterogeneities in radiation dose.

SUPPLEMENTARY INFORMATION

Fig. S1. Regional demarcation of tumor boundaries and vessel segmentation. Panel A: Fluorescence reporter images were used to identify the tumor boundary (red line). Panel B: From this, regions of tumor-associated normal tissue, tumor rim and tumor core were defined according to their distance from the tumor boundary. Within each of these regions, fluorescence signal was quantified. Additionally, vessels were segmented, and Spatially localized vascular parameters were calculated.

Fig. S2. Microbeam radiation effects on vascular function over time. In this single-representative-window chamber, the middle, left and right columns show bright field images, mapped blood flow direction and mapped blood flow speed, respectively. A notable change in vascular orientation was observed. Here vessels initially oriented parallel to the beam length were replaced by vessels running perpendicular to the irradiation portion of the tumor. Blood flow analysis showed no apparent loss of vascular function within the window after microbeam irradiation, as indicated by the detection of normal microvessel blood velocities.

Fig. S3. Histological analysis of extracted tumors. After tumor extraction on day 7, the tumors were preserved and histologically assessed using H&E staining (panels A, B and C photomicrographs at 5× magnification, 400 μm scale bar; panel D photomicrograph at 20× magnification, 100 μm scale bar). Panel A: In the mock group, central, patchy necrosis was observed within the tumor core (arrows). Panel B: The wide-field group showed more widespread damage, with a large number of pleomorphic irregular cells, bizarre mitotic figures and multinucleated cells. Panel C: The microbeam treated tumors showed two distinct neoplastic phenotypes. Radiation-damaged cells were primarily observed within the linear regions corresponding to the microbeam-treated volume (dashed lines). Panel D: Magnified images of the irradiated region showed an abundance of markedly enlarged, pleomorphic cells with bizarre mitotic figures and multinucleation (arrows).

Fig. S4. A proposed model of tumor response to microbeam versus wide-field irradiation. Microbeam irradiation causes an upregulation in HIF-1 in the nonirradiated portions of the tumor through bystander mechanisms. HIF-1, in turn, potentiates vascular recovery. In contrast, wide-field tumor irradiation results in widespread cell death, which eventually leads to reoxygenation due to decreased oxygen consumptions.

REFERENCES

1. Anderson D, Siegbahn EA, Fallone BG, Serduc R, Warkentin B. Evaluation of dose-volume metrics for microbeam radiation therapy dose distributions in head phantoms of various sizes using Monte Carlo simulations. Phys Med Biol 2012; 57:3223–48.

2. Griffin RJ, Koonce NA, Dings RPM, Siegel E, Moros EG, Bräuer-Krisch E, et al. Microbeam radiation therapy alters vascular architecture and tumor oxygenation and is enhanced by a galectin-1 targeted anti-angiogenic peptide. Radiat Res 2012; 177:804–12.

3. Martinez-Rovira I, Sempau J, Fernandez-Varea JM, Bravin A, Prezado Y. Monte Carlo dosimetry for forthcoming clinical trials in x-ray microbeam radiation therapy. Phys Med Biol 2010; 55:4375–88.

4. Sabatasso S, Laissue JA, Hlushchuk R, Graber W, Bravin A, Bräuer-Krisch E, et al. Microbeam radiation-induced tissue damage depends on the stage of vascular maturation. Int J Radiat Oncol Biol Phys 2011; 80:1522–32.

5. Dewhirst MW, Cao Y, Moeller B. Cycling hypoxia and free radicals regulate angiogenesis and radiotherapy response. Nat Rev Cancer 2008; 8:425–37.

6. Dewhirst MW, Cao Y, Moeller B. Cycling hypoxia and free radicals regulate angiogenesis and radiotherapy response. Nat Rev Cancer 2008; 8:425–37.

7. Dewhirst MW, Oliver R, Tso CY, Gustafson C, Secomb T, Gross JF. Heterogeneity in tumor microvascular response to radiation. Int J Radiat Oncol Biol Phys 1990; 18:559–68.

8. Moon EJ, Brizel DM, Chi JT, Dewhirst MW. The potential role of intrinsic hypoxia markers as prognostic variables in cancer. Antioxid Redox Signal 2007; 9:1237–94.

9. Hockel M, Vorndran B, Schlenger K, Baussmann E, Knapstein PG. Tumor oxygenation: a new predictive parameter in locally advanced cancer of the uterine cervix. Gynecol Oncol 1993; 51:141–9.

10. Dietz A, Vanselow B, Rudat V, Conradt C, Weidauer H, Kallinowski F, et al. Prognostic impact of reoxygenation in advanced cancer of the head and neck during the initial course of chemoradiation or radiotherapy alone. Head Neck 2003;25(1): 50–8.

11. Mayr NA, Wang JZ, Zhang D, Grecula JC, Lo SS, Jaroura D, et al. Longitudinal changes in tumor perfusion pattern during the radiation therapy course and its clinical impact in cervical cancer. Int J Radiat Oncol Biol Phys 2010; 77:502–8.

12. Suzuki Y, Nakano T, Ohno T, Kato S, Niibe Y, Morita S, et al. Oxygenated and reoxygenated tumors show better local control in radiation therapy for cervical cancer. Int J Gynecol Cancer 2006; 16:306–11.

13. Semenza GL. Targeting HIF-1 for cancer therapy. Nat Rev Cancer 2003; 3:721–32.

14. Palmer GM, Fontanella AN, Shan S, Hanna G, Zhang G, Fraser CL, et al. In vivo optical molecular imaging and analysis in mice using dorsal window chamber models applied to hypoxia, vasculature and fluorescent reporters. Nat Protoc 2011; 6:1355–66.

15. Fontanella AN, Schroeder T, Hochman DW, Chen RE, Hanna G, Haglund MM, et al. Quantitative mapping of hemodynamics in the lung, brain, and dorsal window chamber-grown tumors using a novel, automated algorithm. Microcirculation 2013; 20:724–35.

16. Moeller BJ, Cao Y, Li CY, Dewhirst MW. Radiation activates HIF-1 to regulate vascular radiosensitivity in tumors: role of reoxygenation, free radicals, and stress granules. Cancer Cell 2004; 5:429–41.

17. Cao Y, Li CY, Moeller BJ, Yu D, Zhao Y, Dreher MR, et al. Observation of incipient tumor angiogenesis that is independent of hypoxia and hypoxia inducible factor-1 activation. Cancer Res 2005; 65:5498–505.

18. Palmer GM, Fontanella AN, Shan S, Dewhirst MW. High-resolution in vivo imaging of fluorescent proteins using window chamber models. Methods Mol Biol 2012; 872:31–50.

19. Zhang G, Palmer GM, Dewhirst M, Fraser CL. A dual-emissive-materials design concept enables tumour hypoxia imaging. Nature Mater 2009; 8:747–51.

20. Palmer GM, Fontanella AN, Zhang G, Hanna G, Fraser CL, Dewhirst MW. Optical imaging of tumor hypoxia dynamics. J Biomed Opt 2010; 15:066021.

21. Moeller BJ, Cao YT, Li CY, Dewhirst MW. Radiation activates HIF-1 to regulate vascular radiosensitivity in tumors: Role of reoxygenation, free radicals, and stress granules. Cancer Cell 2004; 5:429–41.

22. Sorg BS, Moeller BJ, Donovan O, Cao Y, Dewhirst MW. Hyperspectral imaging of hemoglobin saturation in tumor microvasculature and tumor hypoxia development. J Biomed Opt 2005; 10:44004.

23. Hanna G, Fontanella A, Palmer G, Shan S, Radiloff DR, Zhao Y, et al. Automated measurement of blood flow velocity and direction and hemoglobin oxygen saturation in the rat lung using intravital microscopy. Am J Physiol Lung Cell Mol Physiol 2013; 304:L86–L91.

24. Hadsell M, Zhang J, Laganis P, Sprenger F, Shan J, Zhang L, et al. A first generation compact microbeam radiation therapy system based on carbon nanotube X-ray technology. Appl Phys Lett 2013; 103:183505.

25. Schreiber EC, Chang SX. Monte Carlo simulation of a compact microbeam radiotherapy system based on carbon nanotube field emission technology. Med Phys 2012; 39:4669–78.

26. Hadsell MJ. The development and characterization of a first generation carbon nanotube x-ray based microbeam radiation therapy system [Dissertation]. Chapel Hill (NC): University of North Carolina at Chapel Hill; 2013. Available from: http://bit.ly/1BNCBHu.

27. Hadsell M, Ger R, Inscoe C, Schreiber E, Lu J, Chang S, et al. Dosimetric characterization of a prototype nanotechnology microbeam radiation therapy device using Gafchromic EBT2 film (Conference abstract SU-D-144-06; AAPM 55th Annual Meeting, 2013 Aug 4–8; Indianapolis, IN). Med Phys 2013; 40:117. Available from: http://bit.ly/1uRM0c7.

28. Morgan WF. Non-targeted and delayed effects of exposure to ionizing radiation: II. Radiation-induced genomic instability and bystander effects in vivo, clastogenic factors and transgenerational effects. Radiat Res 2003; 159:581–96.

29. Morgan WF. Non-targeted and delayed effects of exposure to ionizing radiation: I. Radiation-induced genomic instability and bystander effects in vitro. Radiat Res 2003; 159:567–80.

30. Dayal D, Martin SM, Limoli CL, Spitz DR. Hydrogen peroxide mediates the radiation-induced mutator phenotype in mammalian cells. Biochem J 2008; 413:185–91.

31. Hei TK, Zhou H, Ivanov VN, Hong M, Lieberman HB, Brenner DJ, et al. Mechanism of radiation-induced bystander effects: a unifying model. J Pharm Pharmacol 2008; 60:943–50.

32. Li F, Sonveaux P, Rabbani ZN, Liu S, Yan B, Huang Q, et al. Regulation of HIF-1alpha stability through S-nitrosylation. Mol Cell 2007; 13(26):63–74.

33. Bonello S, Zähringer C, BelAiba RS, Djordjevic T, Hess J, Michiels C, et al. Reactive oxygen species activate the HIF-1α promoter via a functional NFκB site. Arterioscler Thromb Vasc Biol 2007; 27:755–61.

34. Garcia-Barros M, Paris F, Cordon-Cardo C, Lyden D, Rafii S, Haimovitz-Friedman A, et al. Tumor response to radiotherapy regulated by endothelial cell apoptosis. Science 2003; 300:1155–9.

35. Suit HD, Willers H. Comment on ''Tumor response to radiotherapy regulated by endothelial cell apoptosis'' (I). Science 2003; 302:1894; author reply 1894.

36. Paris F, Fuks Z, Kang A, Capodieci P, Juan G, Ehleiter D, et al. Endothelial apoptosis as the primary lesion initiating intestinal radiation damage in mice. Science 2001; 293:293–7.

37. Brown M. What causes the radiation gastrointestinal syndrome?: Overview. Int J Radiat Oncol Biol Phys 2008; 70:799–800.

38. Ogawa K, Boucher Y, Kashiwagi S, Fukumura D, Chen D, Gerweck LE. Influence of tumor cell and stroma sensitivity on tumor response to radiation. Cancer Res 2007; 67:4016–21.

39. Gerweck LE, Vijayappa S, Kurimasa A, Ogawa K, Chen DJ. Tumor cell radiosensitivity is a major determinant of tumor response to radiation. Cancer Res 2006; 66:8352–5.

40. Ahn GO, Brown JM. Matrix metalloproteinase-9 is required for tumor vasculogenesis but not for angiogenesis: role of bone marrow-derived myelomonocytic cells. Cancer Cell 2008; 13:193–205.

41. Brauer-Krisch E, Serduc R, Siegbahn EA, Le Duc G, Prezado Y, Bravin A, et al. Effects of pulsed, spatially fractionated, microscopic synchrotron X-ray beams on normal and tumoral brain tissue. Mutat Res 2010; 704:160–6.

42. Martínez-Rovira I, Sempau J, Prezado Y. Monte Carlo-based dose calculation engine for minibeam radiation therapy. Physica Medica 2014; 30:57–62.

43. Dilmanian FA, Button TM, Le Duc G, Zhong N, Peña LA, Smith JA, et al. Response of rat intracranial 9L gliosarcoma to microbeam radiation therapy. Neuro Oncol 2002; 4:26–38.

44. Braeuer-Krisch E, Serduc R, Siegbahn EA, Le Duc G, Prezado Y, Bravin A, et al. Effects of pulsed, spatially fractionated, microscopic synchrotron X-ray beams on normal and tumoral brain tissue. Mutat Res 2010; 704:160–6.

45. Dilmanian FA, Rusek A, Fois GR, Olschowka J, Desnoyers NR, Park JY, et al. Interleaved carbon minibeams: An experimental radiosurgery method with clinical potential. Int J Radiat Oncol Biol Phys 2012; 84:514–9.

46. Dilmanian FA, Jenkins III AL, Olschowka JA, Zhong Z, Park JY, Desnoyers NR, et al. X-ray microbeam irradiation of the contusion-injured rat spinal cord temporarily improves hind-limb function. Radiat Res 2012; 179:76–88.